

N. Goldstein, M. Fox, S. Adler-Golden, and B. Gregor, Infrared adaptive spectral imagers for direct detection of spectral signatures and hyperspectral imagery, Proc. SPIE 8618, Emerging Digital Micromirror Device Based Systems and Applications V, 86180D (2013)

Copyright 2014 Society of Photo-Optical Instrumentation Engineers. One print or electronic copy may be made for personal use only. Systematic reproduction and distribution, duplication of any material in this paper for a fee or for commercial purposes, or modification of the content of the paper are prohibited.

<http://dx.doi.org/10.1117/12.2007029>

See next page.

Infrared adaptive spectral imagers for direct detection of spectral signatures and hyperspectral imagery

Neil Goldstein*, Marsha Fox, Steven Adler-Golden, and Brian Gregor
Spectral Sciences, Inc, 4 Fourth Ave. Burlington MA, 01803

ABSTRACT

Field test results are presented for a prototype long-wave adaptive imager that provides both hyperspectral imagery and contrast imagery based on the direct application of hyperspectral detection algorithms in hardware. Programmable spatial light modulators are used to provide both spectral and spatial resolution using a single element detector. Programmable spectral and spatial detection filters can be used to superimpose any possible analog spectral detection filter on the image. In this work, we demonstrate three modes of operation, including hyperspectral imagery, and one and two-dimensional imagery using a generalized matched filter for detection of a specific target gas within the scene.

Keywords: Spectral imager, hyperspectral, DMD, MES, infrared, long-wave, chemical imaging, thermal infrared

1. INTRODUCTION

A prototype Adaptive Multiplexed Spectrograph (AMS) instrument has recently been demonstrated in preliminary field tests. The AMS is the first implementation of a new class of long-wave infrared adaptive spectral imagers that provide passive standoff detection with programmable spatial and spectral resolution. It uses a single photo-detector and an addressable micromirror array to provide both hyperspectral imagery and chemical-specific contrast imagery. Figure 1 illustrates AMS use for chemical standoff detection. The AMS images a one-dimensional (1D) field of view, dividing it into user-selectable spatial resolution units. The system can collect hyperspectral data from the scene or apply a detection filter in hardware to image a specific chemical in the remote cloud. The system, which has no macro-scale moving parts, uses the programmable micromirror array to mask off a specific combination of spectral bands and spatial locations. Using time-multiplexing, it cycles through a number of masks in sequence to produce a 1D spatial image with a user-selected spectral pass band, or a complete hyperspectral image. The system can change the mode of operation and the resolution instantaneously on-the-fly under computer control, and thus can be adapted to a variety of surveillance and monitoring operations.

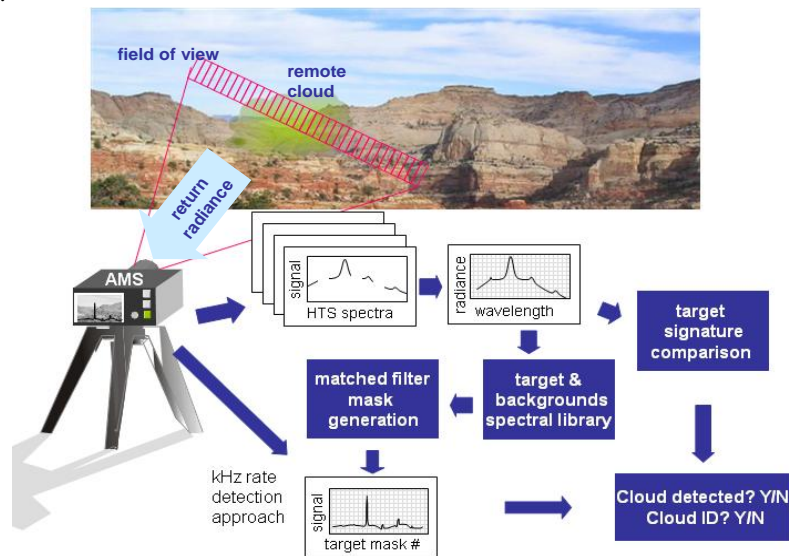


Figure 1. AMS concept.

The method of operation has been described in previous papers.¹⁻³ The AMS, belongs to a class of sensors that disperse the light onto a micromirror array and then combine the selected spatial and spectral bands onto a detector.¹⁻⁶ Most previous authors have concentrated on the ability of such adaptive spectral imagers to produce hyperspectral imagery using Hadamard Transform spectroscopy⁷. In this work we demonstrate both this mode of operation, and the use of the AMS to implement an analog detection filter for imaging a specific gas, R134 (1,1,1-trifluoroethane), in the presence of structured spectral backgrounds. The detection filter is implemented in just two spectral masks, improving device throughput and signal-to-noise ratio (SNR). This ability can be extended to implement any linear detection filter in hardware, including spectral filters for principal component decomposition.

The ability to change modes of operation on-the-fly will allow future intelligent systems to cycle through a variety of operation modes for surveillance and monitoring applications. A small fraction of the time can be devoted to collecting detailed spectral background information about the scene. Locally detected backgrounds can be used to continuously update the detection filters, lowering sensitivity to background spectral features.

Outdoor tests were performed in which the prototype was co-aligned a visible bandpass camera with a common aperture and an FTIR sensor. Figure 2 shows the AMS and FTIR Systems during that test. The AMS and FTIR systems were tested for absolute radiometric accuracy and spectral calibration. The spectral data collected by the two systems was equivalent within the accuracy of the instruments, and matched the known spectrum of R134. An external scanning mirror provided a second spatial dimension, enabling collection of 2D spectral imagery. A generalized formalism was developed for matched filter detection using an adaptive spectral imager, and the filter was used to produce 2D detection images of R134 contained within a LWIR-transparent balloon placed in the scene.

Figure 3 shows representative data products for a scene with a balloon containing R134 and Helium was placed in the field of view. Both the high density polyethylene (HDPE) balloon and Helium are LWIR transmissive. The visual image shows the instantaneous FOV of the AMS system. The hyperspectral image data is shown on the right hand side for a scan with six spatial channels and 64 spectral channels. The R134 spectral features are clearly visible in channels 1 and 2. The left hand side shows detection filter scans through the FOV. The FOV is divided into 30 spatial channels. The 2D images in the center show both the detection filter and wideband images generated by scanning the mirror. These images demonstrate the effectiveness of the detection filter approach. R 134 is clearly present in the detection filter image, while the wide-band image shows all the thermal contrast within the scene, indiscriminate of spectral structure.

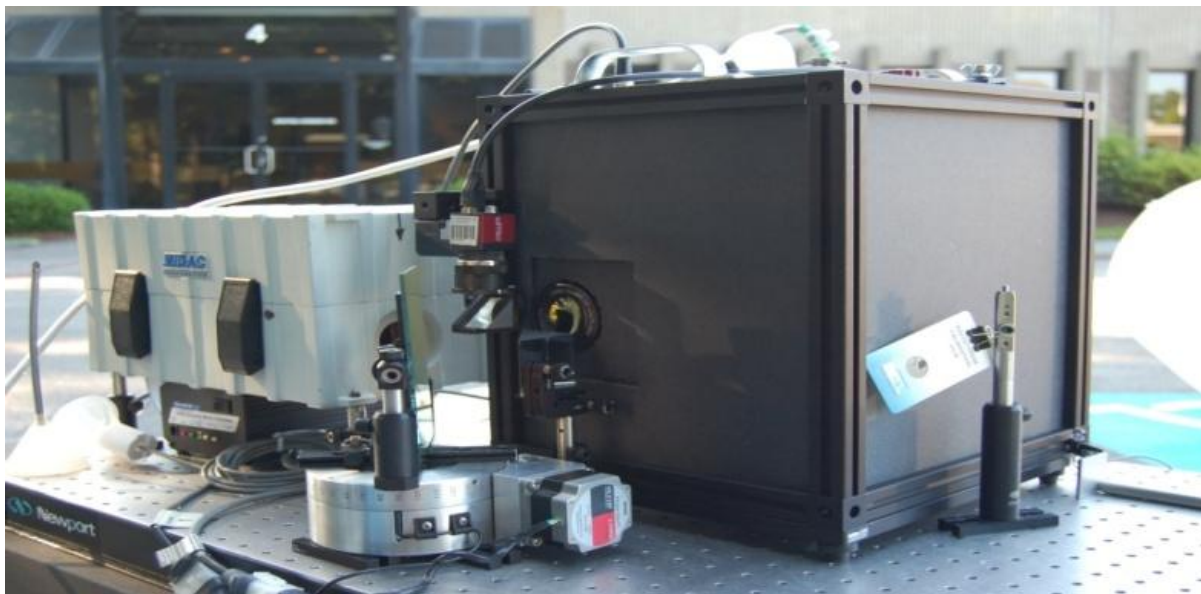


Figure 2. Field test setup. The AMS is on the right, the FTIR on the left.

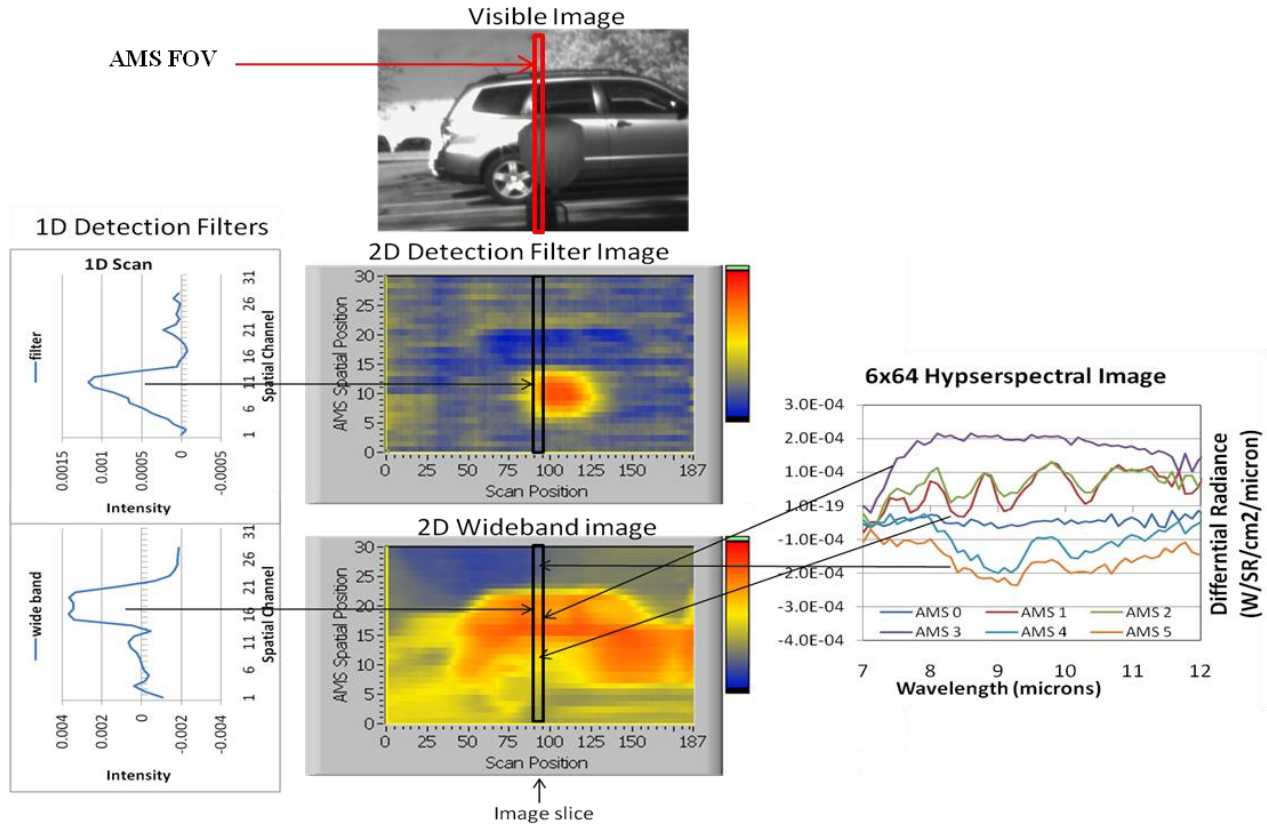


Figure 3. Typical data products from the outdoor tests.

2. AMS PROTOTYPE

Figure 4 shows the basic method of operation of the AMS. The AMS uses a camera lens to produce an image on the input slit of a concave-grating spectrograph represented in the diagram as a prism dispersive element. The spectrograph produces a dispersed image on the Digital Micromirror Device, (DMD), that selects specific spatial and spectral elements and directs them towards a second grating spectrograph that recombines the light and focuses it onto a single detector. The DMD is programmed with a sequence of masks that encode spatial and spectral information. The data processor cycles through the masks and decodes the time sequence data to reconstruct the spectral/spatial image on the DMD in near real time. The frames are cycled at a rate of 13kHz. The Spectral range is 6.5-12.5 microns, the spectral resolution is FWHM=0.1 nm, and the spectral bin size can be set by the operator.

The optical system shown in Figure 5 uses a set of $f/2$ machined gratings⁸ that are 85% efficient at the peak wavelength, a standard IR camera lens, and a Texas Instruments DMD and electronics (Discovery 3000). The DMD has been modified with a ZnSe window. The overall system efficiency is 50% at four microns, and 12% at 9 microns. The lower efficiency in the LWIR is due to diffraction effects from the 13micron square micromirrors and could be improved to match the 4 micron performance if larger mirrors were used.

Different types of masks are applied to the DMD for different operating modes. A series of orthogonal binary masks conforming to the Hadamard simplex are used to encode an entire hyperspectral image. The prototype AMS is capable of up to 64 spectral channels. Alternatively, analog spectral filters can be implemented using a set of grey scaled masks. As shown in Figure 6, a spatial contrast image is obtained using the product of a spatial Hadamard encoding mask and an analog filter encoding mask. The analog filter is implemented as two masks, one for the positive part of the filter and one for the negative part of the filter. These are multiplied by the spatial Hadamard masks to produce two sets of spatial masks that are applied in sequence and decoded to produce a 1D detection image. The signal through the negative spectral mask is subtracted from that of the positive spectral mask to form the detection filter. The weighted sum of the two masks creates the wide band image.

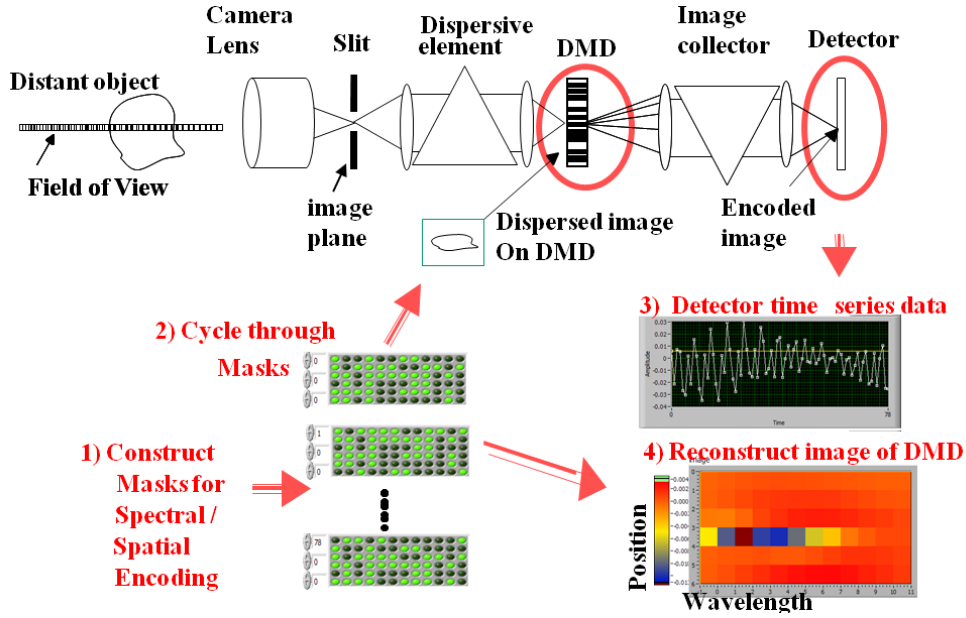


Figure 4. Schematic of operating principles.

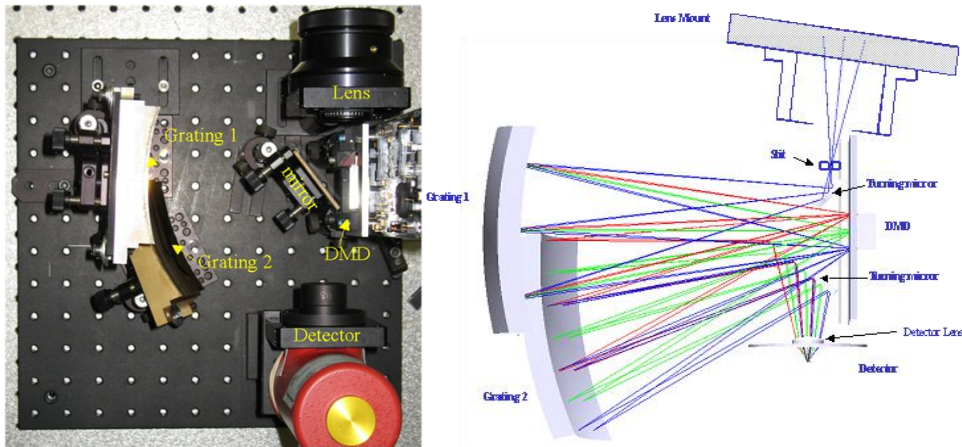


Figure 5. Optical layout. Left- Photograph, right ray trace

Figure 7 shows the implementation for a generalized matched filter for R134 in the presence of hot and cold blackbodies.

The formalism of the generalized matched filter was described previously¹. Briefly stated it is the filter, h , that maximizes the SNR:

$$\text{SNR}^2 = h^T s s^T h / (h^T R h + C^2) \quad (1)$$

Where s is the target spectrum, R is the covariance of the local background spectra, the superscript T denotes the transpose, and C is the component of the detector noise that is independent of the spectral resolution. The solution for a post-processing filter using a standard hyperspectral imager, where $C=0$, is the standard matched filter (for mean subtracted data) or Constrained Energy Minimization filter, CEM (for non-mean subtracted data). In that case there is a dedicated detector for each spectral channel, and the detector noise scales with the signal and is therefore included in the covariance matrix R . In the AMS, where the noise is independent of the resolution, all of the detector noise appears in the term C , rather than R . This results in a different optimum filter, called the generalized filter, which can be derived by numerical solution of Equation 1. Figure 7 shows both the classic CEM filter and the generalized filter for R134 gas. Note that the generalized filter has greater throughput and improves the signal to noise ratio by more than a factor of two relative to the classic matched filter.

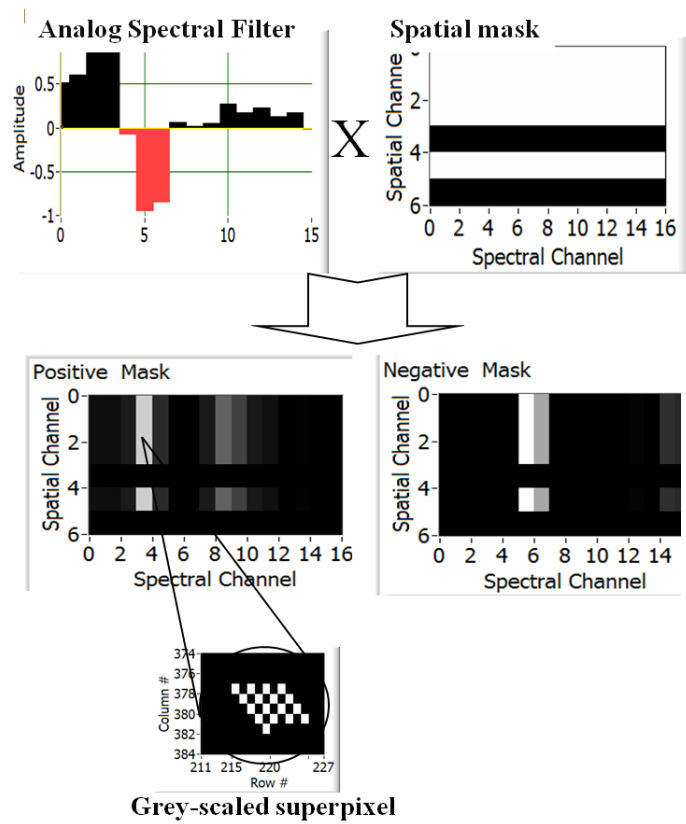


Figure 6. Construction of positive and negative masks for application of an analog spectral filter in a spatial Hadamard scan.

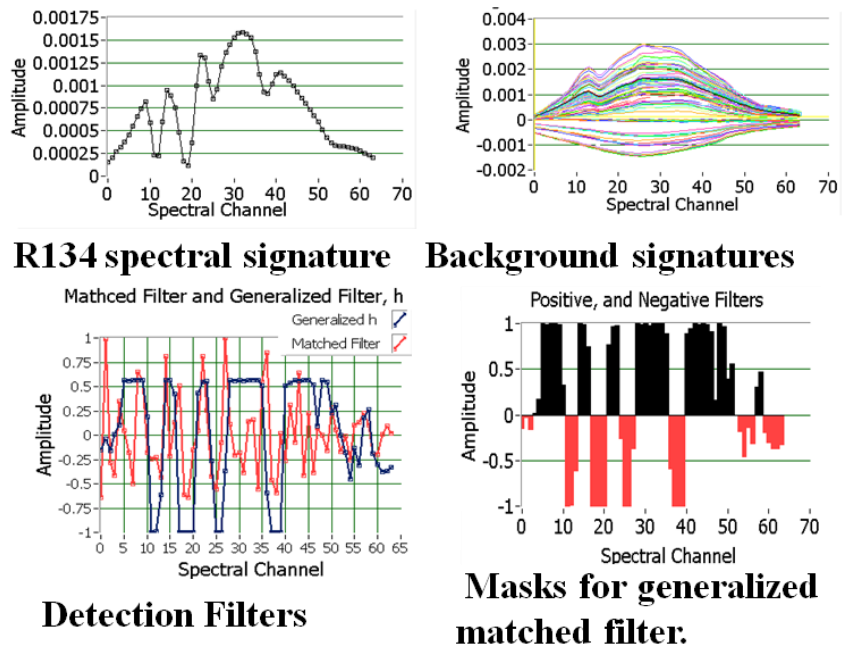


Figure 7. Generalized detection filter for R34.

3. FIELD TESTS

The AMS prototype was mounted on a mobile platform along with a MIDAC FTIR, and a visible camera as shown in Figures 2 and 8. The three instruments are co-aligned to share a common aperture and a common external scanning mirror. Figure 8 shows a view down the optical axis of the three instruments. The input apertures are visible in the external scanning mirror. The instantaneous FOV of the three instruments is shown in Figure 9. The AMS FOV is $\pm 4.6^\circ$ tall and $\pm 0.43^\circ$ wide. The FTIR FOV is $\pm 1.5^\circ$. The test platform is also equipped with a portable gas cell with HDPE windows that can fill the FOV of both instruments, a calibrated 400K blackbody, and a polystyrene calibration standard. These are used to verify radiometric and spectroscopic calibration of the instruments.

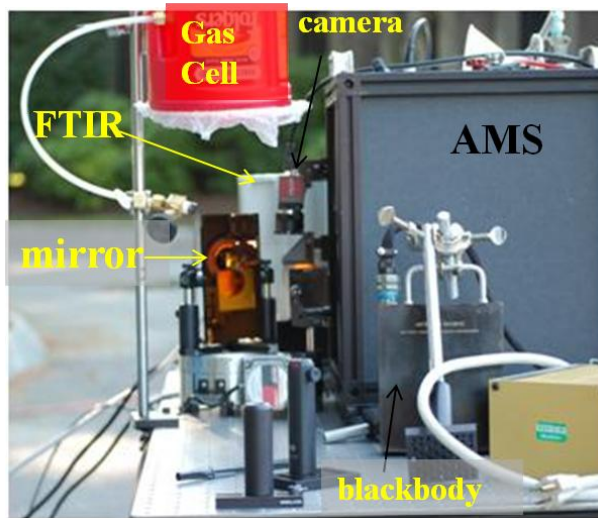


Figure 8. View of test platform along the optical axis.

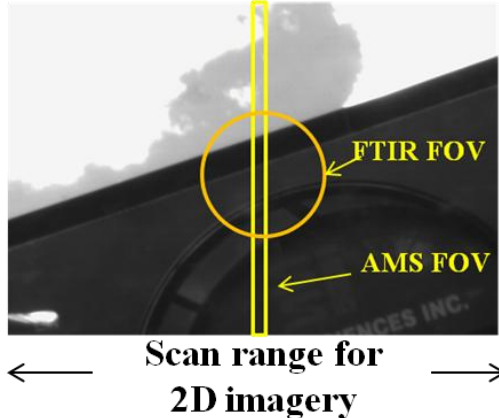


Figure 9. FOV of the instruments.

3.1 Spectral and radiometric calibration

The AMS system measures the differential radiance between the scene and an internal blackbody located on the shutter. Figure 10 shows a typical set of raw spectra for the AMS viewing a 400 K blackbody through a gas cell containing R132 gas. Figure 10 also shows the instrument function, which is calculated for each of the spectral channels using the difference in signal between 400 K and 298 K blackbodies.

The AMS signals are converted to differential radiance signals by dividing by the response function. The differential FTIR signals are obtained by subtracting the FTIR target signal from that of an ambient temperature blackbody and then smoothing the FTIR signal to match the AMS resolution and spectral grid and dividing by the response function. Figure 11 shows typical FTIR and AMS raw signals for a cold sky image. The corresponding differential radiance spectra are shown in Figure 12. The six AMS channels and the FTIR channel all measured approximately the same

spectrum, as they all view a cold sky scene with minimal clouds. Figure 12 compares the mean and standard deviation of the AMS spectra to the FTIR spectrum. The variation in the various AMS channels is of the same magnitude as the deviation from the FTIR spectrum. Figure 13 compares the signals from a 400 K blackbody. The six AMS channels match the theoretical spectrum to better than +/-2%, with the main difference being a structured feature at 7.8 microns corresponding to the SiO₂ coating on the external scanning mirror. The FTIR does not do as well, as the FTIR instrument calibration has some systematic errors in it. Thus, the two instruments have the same spectral and radiometric calibration within the accuracy of the sample preparation and the calibration of the FTIR.

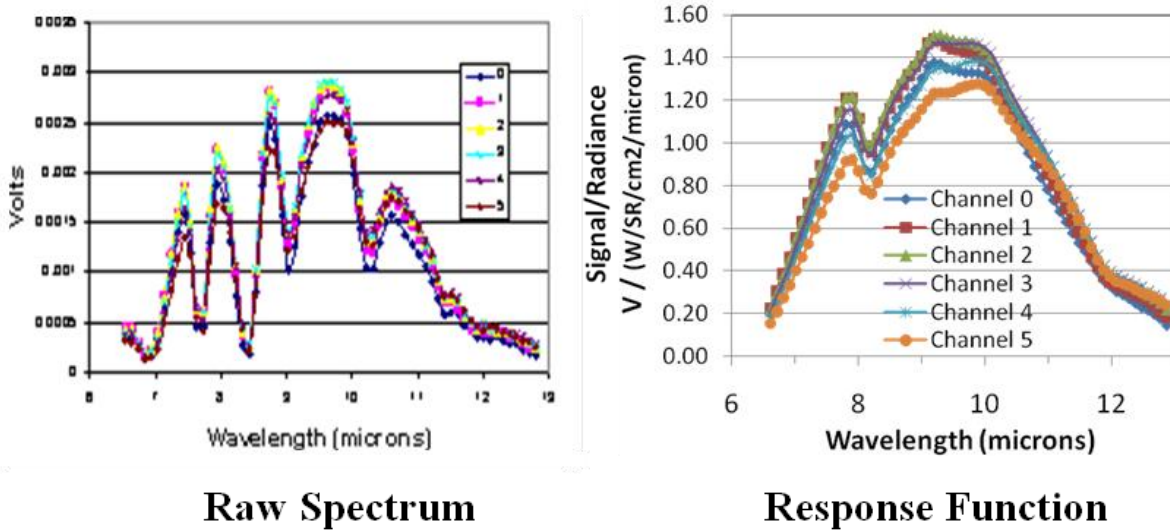


Figure 10. Raw AMS signals for R134 absorption of 400K blackbody radiation.

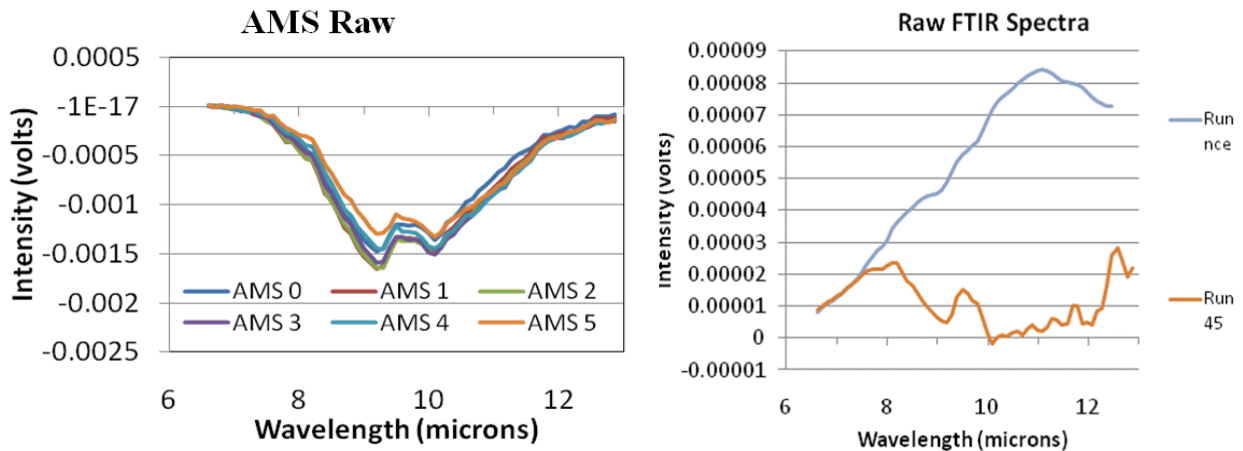


Figure 11. Raw sky spectra for AMS and the FTIR.

Figure 14 shows a series of measurements of R134 against a cold sky background with a variety of optical depths in the absorption cell. The data were processed to produce transmission spectra and then compared to the known spectrum of R134 from the PNNL spectral data base⁹. Figure 15 shows the comparison for one such data set. The FTIR data and PNNL data are smoothed and re-sampled onto the spectral grid of the AMS, using the known slit function of the AMS. The resulting data for the AMS and FTIR match very well, and fit the theoretical spectrum for a column density of 450 ppm-m R134. The PNNL data fit diverges substantially at 6.7 microns, but this may be due to the absorption of the cell windows in this wavelength range, which makes the measurement uncertainties quite large in this region.

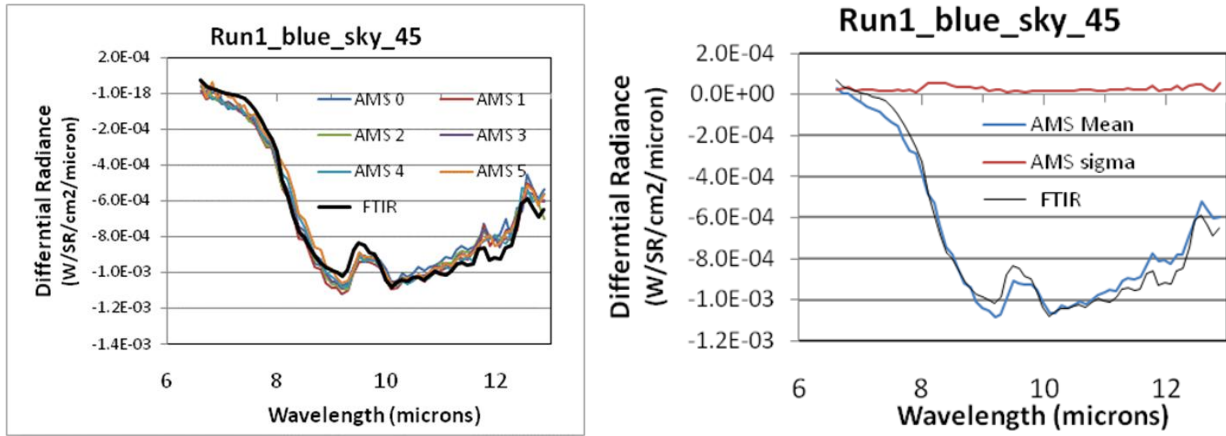


Figure 12. Comparison of calibrated differential radiance. Left – Six AMS channels and FTIR, Right AMS mean and sigma and FTIR.

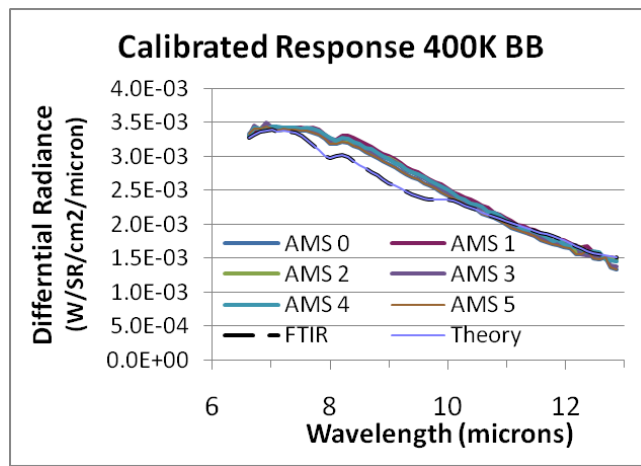


Figure 13. Comparison of response to calibrated blackbody.

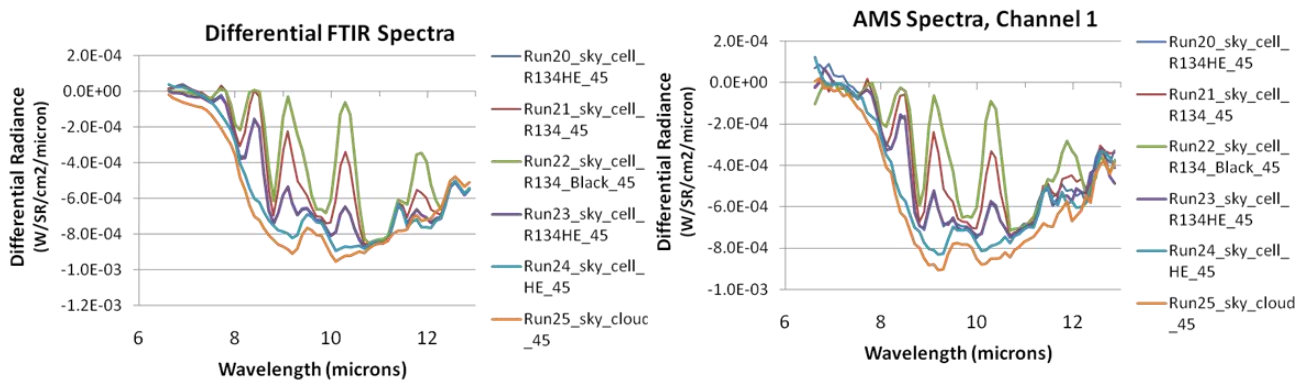


Figure 14. Differential spectral for R134 against a Blue Sky Background.

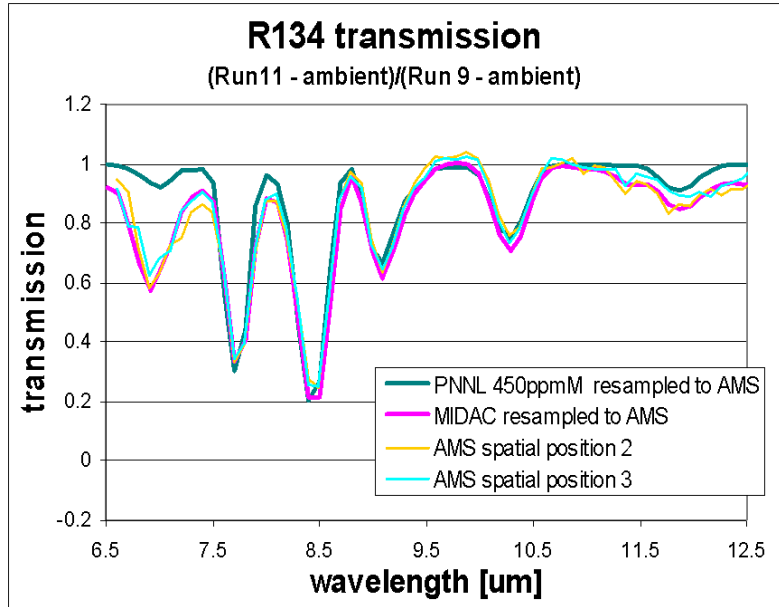


Figure 15. Comparison of AMS and FTIR transmission spectra to the PNNL data base.

3.2 Chemical detection imagery

Figure 16 shows typical detection imagery produced using the R134 generalized detection filter of Figure 7. HDPE bags, originally designed for dry cleaning, are filled with a mixture of He and R134 or pure He and placed within the field of view. 1D spatial detection filter scans are taken at a rate of 230 Hz while scanning the external mirror. The 1D images are then registered with the mirror scan to produce 2D images. The detection images are converted to an apparent contrast temperature averaged over the full 6.5-12.5 micron spectral range of the AMS. The wide band images are also presented in terms of apparent contrast temperatures.

Figure 16 shows data taken with and without an R134 target in the field of view of the AMS. The contrast temperature in the wide band image ranges from -5 to 17K, with a contrast temperature of about 15 K for the building that is prominent in the field of view. The detection filter image shows R134 with a contrast temperature of about 3 degrees. In the absence of R134, the detection filter response is zero.

Figure 16 also shows 2D contrast images obtained by sweeping the external scanning mirror through 9 degrees once per second. The resulting 2D images match the instantaneous field of regard of the visible camera. The 2D detection filter images show a clear outline of the R134 target and are nearly featureless in the absence of R134. The wide band images show the temperature contrast of the scene, with a cold sky, moderately warm vegetation, and a hot building.

Figure 17 illustrates how the contrast temperature signal of the R134 varies with the temperature of the background. The R134-containing balloon is moved across the field of view and is observed against pavement, distant vegetation and different parts of a car. The strength of the R134 image tracks the temperature contrast between the R134 with the background. Note also that while the detection filter images are nearly flat in the absence of R134, there is a small amount of response to window glass and car paints as the spectral signature of these materials were not included in the background spectra used to define the detection filter. Inclusion of such local backgrounds in a revised filter would result in no false-alarm response to these materials.

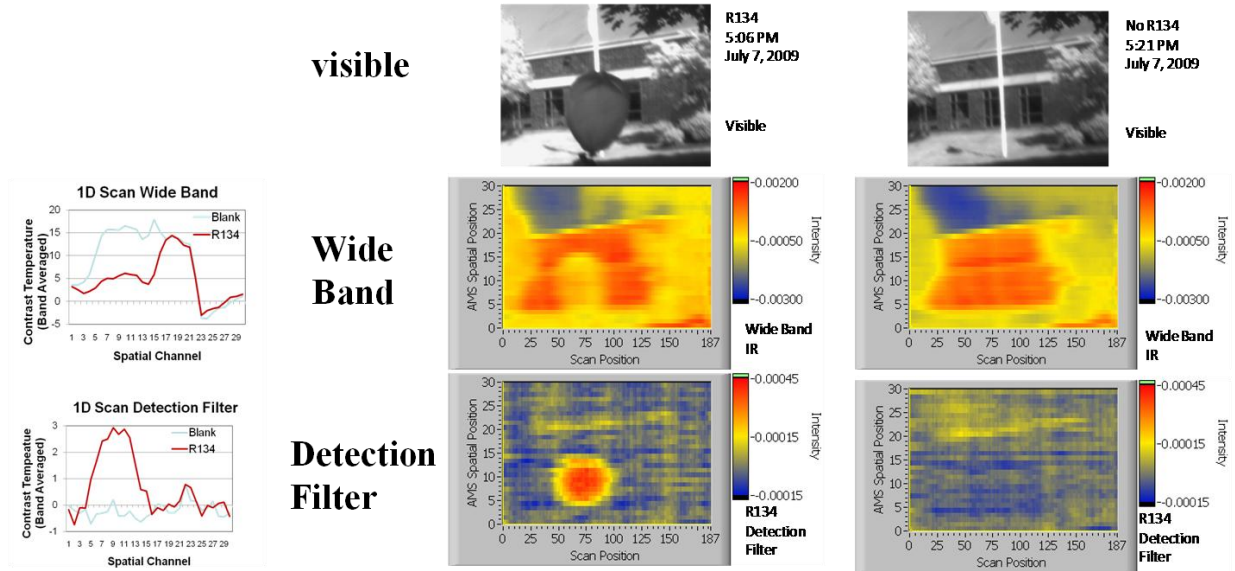


Figure 16. Detection imagery with and without R134.

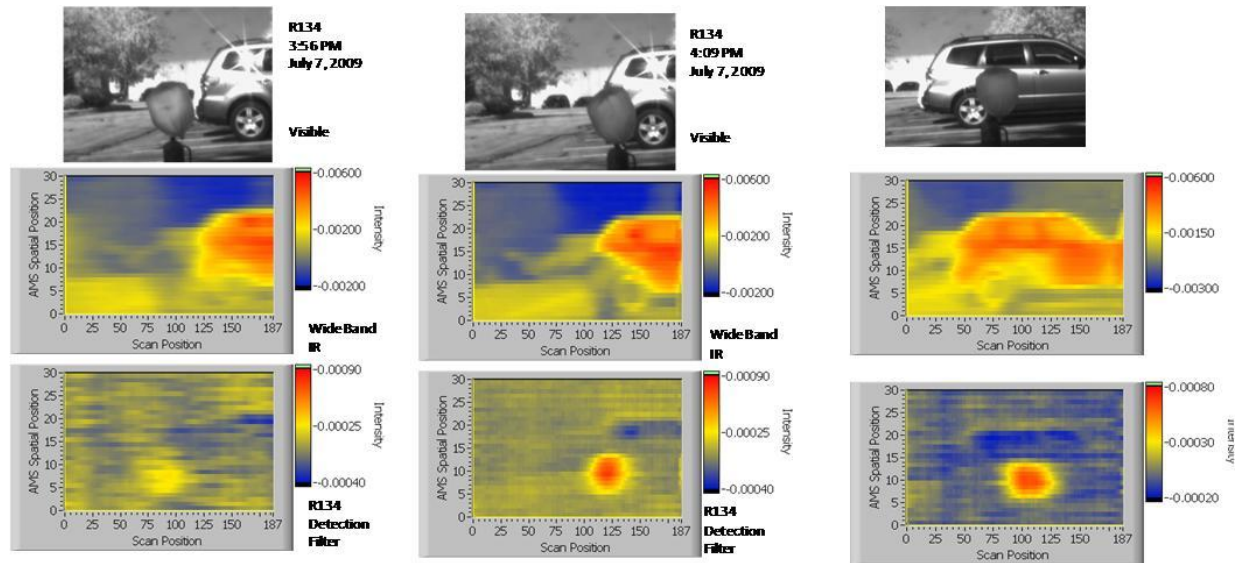


Figure 17. Detection Imagery as a function of background.

3.3 Detection Sensitivity

The detection sensitivity of the AMS system was measured in a variety of circumstances and seen to exactly match the theoretical efficiency, based on the known transmission efficiency of the components, the $f/2$ collection optics, and the detector noise characteristics. The SNR depends on the number of spectral and spatial bands measured and the amount of averaging time. Table 1 reports typical values for Noise Equivalent Power, NEP, Noise Equivalent Spectral Radiance, NESR, and Noise Equivalent Difference Temperature, NEDT, for different operating modes, frame rates, and resolution. For a hyperspectral measurement the SNR can be characterized by the NESR in each spectral band. The noise limit for the prototype is $\text{NESR}/\text{Hz}^{1/2}/\text{band} = 3 \times 10^{-8} \text{ W/Sr/micron/cm}^2/\text{Hz}^{1/2} \text{ band}$. The NESR scales linearly with the number of bands and as the square root of the data rate. Thus for example, the NESR is $1 \times 10^{-6} \text{ W/Sr/micron/cm}^2$, or 1 microFlick, for 30 spatial/spectral bands collected at a 1Hz frame rate. For a full 6×64 hyperspectral image, data must be collected for 100 seconds ($F=0.01 \text{ Hz}$), to reach the same NESR. For a detection filter, the signal is integrated over the spectral band of the target gas and is expressed as an NEP. The NEP value is given by $\text{NEP}/\text{Hz}^{1/2}/\text{band} = 1 \times 10^{-7} \text{ W/SR/cm}^2/\text{Hz}^{1/2}/\text{band}$. This can also be expressed as an equivalent temperature differential as averaged over the 6.6-12.5 micron band; the $\text{NEDT}/\text{Hz}^{1/2}/\text{band} = 0.001 \text{ K}/\text{Hz}^{1/2}/\text{band}$.

It should be stressed these values are not the limiting value for the technology, but rather are the values for the prototype as built. The SNR can be improved by a factor of 12 with improved components. Specifically, the detector noise can be reduced by a factor of three by using a rectangular detector with an appropriate sized cold stop, and the system throughput can be increased by a factor of four, either by using larger DMD micromirrors in the long-wave infrared spectral region, or using the same DMD micromirrors in the mid-wave infrared where they are nearly 100% efficient.

Table 1. Noise equivalent power.

Mode	Resolution	Frame rate	NEP/NESR	NEDT
Hyperspectral	6x64	1Hz	1.4×10^{-5} W/SR/Cm ² /Micron	0.8°K
	2x32	1 Hz	1.0×10^{-6} W/SR/Cm ² /Micron	0.06°K
Detection Filter	30	50 Hz	4×10^{-5} W/SR/Cm ²	0.3°K
	30	1 Hz	6×10^{-6} W/SR/Cm ²	0.04°K

4. CONCLUSIONS, DISCUSSION, AND FUTURE PLANS

These field test results demonstrate the capabilities of adaptive spectral imagers for direct chemical contrast imagery and for hyperspectral image generation. A single-detector system can produce 1D-spectral and 1D-spatial hyperspectral imagery and implement direct detection of a chemical in the presence of background interferents. The system provides spectral data with absolute spectral and radiometric calibration. Signal-to-noise performance is consistent with a first principles analysis based on the throughput and efficiency of the optical components.

The prototype system can serve as the basis of the next generation of portable standoff detection monitors. It is inherently robust, having no macro-scale moving parts, and is thus well suited for operation on-the-move in mobile platforms and in hostile environments. The prototype as tested provides spectral detection with a sensitivity that approaches that of current systems such as the JSLSCAD. With further engineering improvements, it can surpass that sensitivity. Its greatest advantage is the ability to provide spatially resolved information to help with chemical detection and identification. This spatial information can be obtained with a single detector, which suggests that the cost for a commercial sensor would be much lower than existing hyperspectral instrumentation. Furthermore, the unique capabilities to perform sensitive chemical detection in hardware suggest a wide range of new and improved detection algorithms that can be accomplished with adaptive spectral imagers. The system can form the basis of a flexible and adaptable standoff detection system. A single system can operate in a number of operating modes and change between them on-the-fly and in real time.

In future work, we anticipate the development of automated surveillance and detection algorithms that take advantage of the various operating modes of the system, and the engineering development of adaptive spectral sensors for field applications. This includes the hardening and shrinking of the detector package, and the development of 2D imaging hardware without the use of an external scanning mirror.

ACKNOWLEDGMENTS

The Authors gratefully acknowledge the Defense Threat Reduction Agency (DTRA), and our technical monitors, Donald Cronce and Morgan Sparks for supporting this work, which was supported under the following contracts: Chemical/Biological Agent Standoff Detection, HDTRA1-05-P-0126 (DTRA), Don Cronce TPOC; TRACER Detection System Phase III BAA, HDTRA3-12-C-0095, Morgan Sparks TPOC.

REFERENCES

- [1] Goldstein, Neil, Pajo Vujkovic-Cvijin, Marsha Fox, Brian Gregor, Jamine Lee, Jason Cline, and Steve Adler-Golden “DMD-based adaptive spectral imagers for hyperspectral imagery and direct detection of spectral signatures,” SPIE Vol. 7210,721008-1-721008-8 (2009).
- [2] Goldstein N., Pajo Vujkovic-Cvijin; Marsha Fox; Steven Adler-Golden; Jason Cline; Brian Gregor; Jamine Lee; Alan C. Samuels; Shawn D. Higbee; Latika S. Becker; Teng Ooi, “Programmable Adaptive Spectral Imagers for Mission-Specific Application in Chemical/Biological Sensing, International Journal of High Speed Electronics and Systems (IJHSES)”, Volume: 17, Issue: 4 Page. 749 - 760 (2007).
- [3] Vujkovic-Cvijin, P., Goldstein, N., Fox, M.J., Higbee, S.D., Latika S. Becker L.C., and Teng K. Ooi, T.K. “Adaptive Spectral Imager for Space-Based Sensing,” Proc. SPIE Vol. 6206, paper 6206-33 (2006).
- [4] Goldstein, N., P. Vujkovic-Cvijin, M. J. Fox, S. Adler-Golden, J. Lee, J.A. Cline, B. Gregor, “Spectral Encoder,” US Patent 7,324,196 (2008).
- [5] Wehlburg, C.M., Wehlburg, J.C., Gentry, S.M., and Smith, J.L, “Optimization and characterization of an imaging Hadamard spectrometer,” Proc. SPIE Vol. 4381, p. 506-515, Algorithms for Multispectral, Hyperspectral, and Ultraspectral Imagery VII, Sylvia S. Shen, Michael R. Descour, Eds., (2001)
- [6] Wuttig, A. and R. Riesenber, “Sensitive Hadamard Transform Imaging Spectrometer with a simple MEMS,” Proc. SPIE, 4881, pp. 167-178, (2003).
- [7] Harwit, M. and N.J.A. Sloane, Hadamard Transform Optics, Academic Press, NY, (1979).
- [8] Manufactured by Headwall Photonics.
- [9] Sharpe, S. W., T. J. Johnson, R. L. Sams, P. M. Chu, G. C. Rhoderick, P. A. Johnson, Gas-phase database for quantitative infrared spectroscopy, App. Spec, Vol: 58, no. 12, pp. 1452-1461, (2004).